Applied Catalysis B: Environmental 244 (2019) 459–464

Contents lists available at ScienceDirect

Applied Catalysis B: Environmental

journal homepage: www.elsevier.com/locate/apcatb

Enhanced electron separation on in-plane benzene-ring doped g-C_3N_4 nanosheets for visible light photocatalytic hydrogen evolution

Jian Liu[a,b], Yu Yu[c], Ruilian Qi[a,b], Changyan Cao[a,b,*], Xiaoyan Liu[d], Yujun Zheng[d], Weiguo Song[a,b,*]

[a] Beijing National Laboratory for Molecular Sciences, Laboratory of Molecular Nanostructures and Nanotechnology, CAS Research/Education Center for Excellence in Molecular Sciences, Institute of Chemistry, Chinese Academy of Sciences, Beijing 100190, China
[b] University of Chinese Academy of Sciences, Beijing 100049, China
[c] School of Science, Beijing Jiaotong University, Beijing 100044, China
[d] School of Physics, Shandong University, Jinan 250100, China

ARTICLE INFO

Keywords:
g-C_3N_4
In-plane
Benzene-ring doping
Hydrogen evolution
Photocatalysis

ABSTRACT

Solar-to-chemical energy conversion by photocatalytic hydrogen evolution (PHE) is critical for reduction of the pollution and storage of clean energy. To improve the solar conversion efficiency, it is highly imperative to accelerate the photocarrier separation and transportation through materials design. Herein, we describe a highly effective PHE catalyst based on in-plane benzene-ring doped g-C_3N_4 nanosheets heterostructure through the thermal co-polymerization of urea and 4, 4'-sulfonyldiphenol (BPS) followed by a controlled heat-etching step. The solid-state ^{13}C NMR confirms the existence of benzene-ring structure in g-C_3N_4 nanosheets. Experimental results and theoretical calculations show that the energy and electronic structure of the catalyst are optimally regulated, inducing increased light absorption and effectively accelerated separation of the photo-driven charge carriers. It exhibits enhanced photocatalytic hydrogen evolution efficiency with a PHE rate of 12.3 mmol h^{-1} g^{-1} (almost 12 times higher than that of pure g-C_3N_4 nanosheets) and the quantum efficiency of 17.7% at 420 nm.

1. Introduction

Solar energy is the prospective renewable alternative for the traditional fossil fuels due to its clean, abundant, and easy-to-get characters. The key issue in this field is to convert and storage solar energy with high efficiency. Solar-to-chemical energy conversion by photocatalytic water splitting is considered as one of the most promising processes since Fujishima and Honda reported the first photocatalytic hydrogen evolution (PHE) reaction on the TiO_2 electrodes in 1972 [1,2]. From then on, numerous kinds of semiconductors were investigated for PHE reactions [3–10]. Recently, graphitic carbon nitride (g-C_3N_4), an outstanding polymeric semiconductor with two-dimension structure, has received significant attention due to its unique electronic and optical properties [11]. Moreover, the outstanding stability, low cost, and facile preparation make g-C_3N_4 a star material in the photocatalytic field [12]. However, pure g-C_3N_4 shows unsatisfactory photocatalytic activity due to its low surface area and poor photoinduced charge separation and mobility.

Peeling bulk materials into thin nanosheets [13–16] and constructing hierarchical nanostructures [17–21] are effective methods to increase the surface area and shorten the transportation distance, leading to enhanced efficiency of photocarrier separation. On the other hand, heteroatom doping [22–27] and heterojunction constructing [28–35] are often used to modify the atomic and electronic structure of g-C_3N_4 to accelerate electron-hole separation and transportation. In particular, integrating aromatic structures into the skeleton of g-C_3N_4 via π-conjugated bond is an effective strategy [36–41].

In this study, we developed a facile method to produce benzene-ring doped g-C_3N_4 nanosheets catalyst (denoted as BS-CN) through thermal co-polymerization of urea and 4, 4'-sulfonyldiphenol (BPS) followed by a controlled heat-etching step. BPS is involved in the polymerization during the melamine formation step, making it an ideal molecular doping agent to g-C_3N_4 nanosheets through co-polymerization (the possible polymerization process of urea and BPS was depicted in Scheme S1). In addition, owing to similar aromatic structure and size, the benzene-ring derivative could be easily incorporated into the g-

* Corresponding authors at: Laboratory of Molecular Nanostructures and Nanotechnology, Institute of Chemistry, Chinese Academy of Sciences, Beijing 100190, China.
E-mail addresses: cycao@iccas.ac.cn (C. Cao), wsong@iccas.ac.cn (W. Song).

https://doi.org/10.1016/j.apcatb.2018.11.070
Received 19 September 2018; Received in revised form 11 November 2018; Accepted 23 November 2018
Available online 24 November 2018
0926-3373/ © 2018 The Authors. Published by Elsevier B.V. This is an open access article under the CC BY-NC-ND license (http://creativecommons.org/licenses/BY-NC-ND/4.0/).

C_3N_4 backbone through sp^2-hybridized C—N bonds [42]. Experimental results and theoretical calculations show that the energy and electronic structure of BS-CN catalyst are optimally regulated, leading to increased light absorption and effectively accelerated separation of the photo-driven charge carriers. The in-plane heterostructured catalyst exhibits enhanced photocatalytic hydrogenation efficiency with a PHE rate of 12.3 mmol h^{-1} g^{-1} (12 times higher than pure g-C_3N_4 nanosheets) and the highest quantum efficiency of 17.7% at 420 nm. Moreover, the catalyst shows satisfied stability even after six cycles in 18 h.

2. Experimental section

2.1. Materials

Urea (99%) was purchased from Beijing Chemical Reagent Company. 4, 4'-Sulfonyldiphenol (BPS, 99%) was provided by Alfa-Aesar. All of the chemicals were directly used as received without further treatment, and the water used through the experiment was from MilliQ system.

2.2. Synthesis of BS-CN

In a typical procedure, 20 g of urea and a certain amount (i.e. 25 mg) of BPS were mixed thoroughly, and then the mixture was loaded into a crucible with a cover. Then the crucible was heated to 550 °C with a heating rate of 2.3 °C/min and kept at this temperature for 4 h. The resulted powder was then transferred to a rectangle crucible without cover for heat etching treatment at 500 °C for 2 h with a heating rate of 10 °C/min in a muffle furnace. After cooling down to room temperature, the as-synthesized samples were directly used for the characterizations and catalytic tests without any of post treatment. In comparison, pure g-C_3N_4 were prepared by the same method without adding BPS. For the synthesis of other control samples, different amount of additives or etching temperature/time were adopted in a similar procedure.

2.3. Characterizations

X-ray diffraction (XRD) patterns were performed on a Rigaku D/max-2500 diffractometer with Cu Kα radiation (λ = 1.5418 Å) at 40 kV and 200 mA. The morphology and microstructures of the samples were characterized by scanning electron microscopy (HITACHI S-4800 SEM), and high-resolution transmission electron microscopy (JEOL, JEM-2100F). EDS mappings of the materials were conducted using scanning TEM (STEM) equipped with an EDS detector (JEOL 2100F). Atomic force microscope (AFM) images and height profiles were acquired through a Nanosurf Flex-Axiom microscope. XPS measurement was performed on the VG Scientific ESCALab220i-XL spectrometer using Al Kα radiation. UV–vis absorption spectra were obtained on Shimadzu UV-2550 spectrophotometer with $BaSO_4$ as a reflectance standard. The specific surface area was measured by the Brunauer-Emmett-Teller (BET) method using N_2 adsorption and desorption isotherms on a JW-BK132F high performance micropore analyzer at 77 K. Raman spectra were collected on LabRAM HR Evolution Raman microscope. Static and time-resolved decay fluorescence spectra were gathered on FLS980 fluorescence spectrometers (λ_{ext} = 370 nm). The ^{13}C cross-polarization magic-angle spinning (CP–MAS) NMR spectra was recorded on the Bruker Avance III 400WB solid-state NMR spectrometer.

2.4. Photocatalytic hydrogen evolution activity

The photocatalytic water splitting reactions were carried out in PerfectLight Labsolar-III AI automatic online photocatalytic analysis system (Beijing Perfectlight Technology Co., Ltd.). 10 mg of photocatalyst was dispersed in a 100 ml aqueous solution containing triethanolamine (10 vol %) as sacrificial electron donors. An appropriate amount of H_2PtCl_6 aqueous solution was added into the photoreactor vessel to depose 3 wt% Pt co-catalyst. The reactant solution and the system were thoroughly evacuated several times to remove air completely. The photocatalytic reaction was triggered by a 300 W Xe lamp (PLS-SXE 300, Beijing Trusttech Co. Ltd, China) with a 420 nm cut-off filter under continuous stirring. The temperature of the reactant solution was maintained at 12 °C by a flow of cooling water during the reaction. The amount of evolved H_2 was analyzed by an online gas chromatography (Fuli GC9790SD, TCD detector). The quantum efficiency (QE) was estimated using the equation: QE (%) = (2 × H/I) × 100, where H and I represent the numbers of evolved H_2 molecules and incident photons, respectively. The light source of QE measurement was a 300 W Xe lamp (PLS-SXE 300, Beijing Trusttech Co. Ltd, China), same as that of the PHE reactions. The number of incident photons (3.8×10^{22} photons h^{-1} at 420–760 nm) was measured using a calibrated Si photodiode. For simplicity, it is assumed that all incident photons are absorbed by the photocatalyst.

2.5. Photoelectrochemical measurements

10 mg of photocatalyst was dispersed in ethanol under sonication. Then a certain amount of Nafion ethanol solution was added and mixed with the suspension to form a homogenous slurry. A certain amount of the slurry was dripped on an L-shape glass carbon electrode (GCE) with the diameter of 4 mm as the working electrode. The loading mass of the photocatalyst was about 0.4 mg cm^{-2}. The photoelectrochemical measurements were carried out in a beaker with a CHI760 electrochemical workstation (CH Instruments, Inc., Shanghai). The photocurrent response was measured in 0.2 M Na_2SO_4 solution at an electrode potential of 0.4 V (vs. Ag/AgCl) in a standard three-electrode system with a Pt net and Ag/AgCl (saturated KCl) used as the counter electrode and reference electrode, respectively. The GCE was irradiated by a 300 W Xe lamp with a 420 nm cut-off filter. Mott-Schottky plots were obtained by three sweeps in a voltage range of −1.5 ~ 1 V with an amplitude of 10 mV at the selected frequencies of 2.9, 1.9, and 1.2 kHz.

2.6. DFT calculations

The calculations were carried out based on density functional theory (hybrid functional, HSE06) using the Vienna ab-initio simulation package (VASP) [43,44]. The generalized gradient approximation (GGA) using the Perdew-Burke-Ernzerhof (PBE) exchange correlation functional was employed, with the cut-off energy of 500 eV, total energy convergence of 1×10^{-4} eV and force convergence of 0.01 eV $Å^{-1}$. A supercell configurations consisting of one doped layer and one undoped layer under the AB stacking rule [45]. The undoped layer was constituted by four pure tri-s-triazene units. In the doped layer, the two benzene rings of diphenylsulfone was located in two neighboring tri-s-triazene units, and the sulfur atom was the connected atom to another tri-s-triazene unit. After the relaxation, the diphenylsulfone doped BS-CN unit cell (14.38 Å × 14.38 Å × 7.35 Å, α = 88.6°, β = 91.6°, γ = 119.7°) exhibited little change compared to the pure g-C_3N_4 (14.27 Å × 14.27 Å × 7.20 Å, α = 90.0°, β = 90.0°, γ = 120.0°). The Monkhorst–Pack scheme K points grid sampling was set as 5 × 5 × 3 for the irreducible Brillouin zone. The band structures were calculated along the paths connecting the following high symmetry points: Γ(0,0,0), A(0.5,0,0), H(0.5,0,0.5), K(0,0,0.5), Γ(0,0,0), M(0,0.5,0), L (0,0.5,0.5), K(0,0,0.5) in the k-space.

3. Results and discussion

3.1. Preparation and characterizations of BS-CN

The morphology of BS-CN was characterized by transmission electron microscope (TEM) and scanning electron microscope (SEM). As shown in Fig. 1a and Figs. S1a–b, BS-CN exhibited homogeneous sheet-

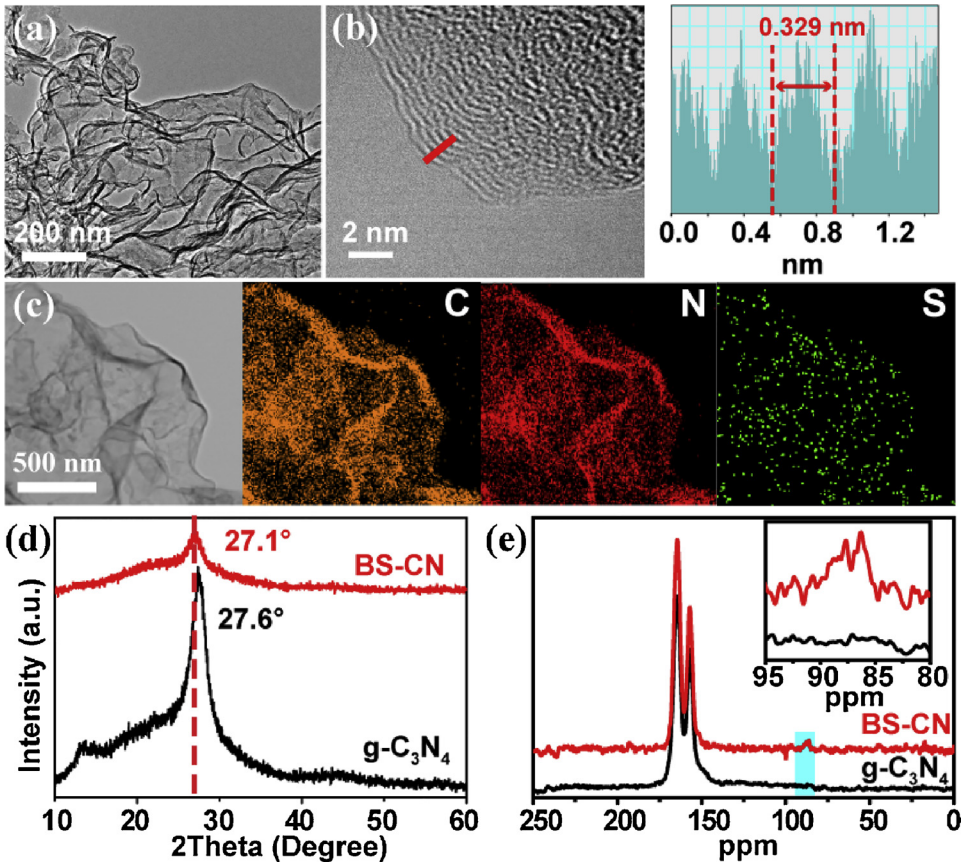

Fig. 1. (a) TEM and (b) HRTEM images of BS-CN, the right image of panel b shows the lattice spaces along the red line in panel b. (c) STEM image and EDS elemental mapping of C, N, and S of BS-CN. (d) XRD patters and (e) solid-state ^{13}C NMR spectra of BS-CN and g-C_3N_4 nanosheets. The inset of (e) shows the magnified spectra of the rectangle region (For interpretation of the references to colour in this figure legend, the reader is referred to the web version of this article).

like structure, similar to that of pure g-C_3N_4 nanosheets. The average thickness was only ~2.8 nm as verified by atomic force microscope (AFM, Figs. S1c–d). EDS elemental mapping (Fig. 1c) clearly showed that sulfur was uniformly distributed throughout the nanosheet, suggesting BPS was homogeneously doped into the g-C_3N_4 nanosheets without self-polymerization. The homogeneousness was further confirmed by the EDS mapping conducted by SEM with an EDS detector (Fig. S2). The high-resolution TEM (HRTEM) image (Fig. 1b) showed the lattice fringes with a spacing of 0.329 nm, which was a little larger than that of the pure g-C_3N_4 nanosheets (~0.325 nm). Since the carbon-ring ingredient was involved in the synthesis process, its polymerization might introduce some coplanar rings within the network of g-C_3N_4 nanosheets, resulting in larger space between layers. The X-ray diffraction (XRD) patterns also confirmed the small change. The representative peak of periodic stacking of layers at 27.6° of g-C_3N_4 shifted to 27.1° in BS-CN (Fig. 1d), indicating the increase of stacking distance. The higher atomic ratio (1.03 vs. 0.92 for g-C_3N_4) of C/N in BS-CN gave another evidence (Table S1) of the benzene-ring doping. The solid-state ^{13}C NMR was further tested to confirm the benzene-ring doping. As shown in Fig. 1e, a new peak at 87 ppm was observed, which can be ascribed to aromatic carbon [46]. The NMR result directly evidenced the existence of benzene ring structure in g-C_3N_4 nanosheets.

N_2 adsorption-desorption measurement (Fig. S4b) showed that the specific surface area of BS-CN was 249.7 $m^2 g^{-1}$, similar to that of pure g-C_3N_4 nanosheets (248.1 $m^2 g^{-1}$). The result indicated that the incorporation of benzene-ring derivative dopants into g-C_3N_4 nanosheets did not reduce the surface area, which is one of the critical factors in the photochemical reaction.

XPS spectra were then used to analyze the surface structure of BS-CN. In the C 1s XPS spectrum of BS-CN (Fig. 2a), the main peak at 284.8 eV was ascribed to graphite sp^2 carbon, which was derived from the benzene ring; for comparison, g-C_3N_4 showed the main peak at 288.2 eV corresponding to the N—C=N sp^2 carbon [47,48]. The N 1s XPS spectra (Fig. 2b) of the both two samples showed similar characters, except for a weaker bridging tertiary N peak (400.0 eV) of BS-CN, indicating that BPS doping can distort the periodicity of g-C_3N_4 to some extent [47]. The main peak was located at 398.6 eV, which originated from the hybridized sp^2 aromatic N in the triazine ring [13]. The weak peaks at 401.1 eV, referred to amino functional group, were also same for g-C_3N_4 and BS-CN [42]. The O 1s XPS spectrum (Fig. 2c) of BS-CN could be deconvoluted into two peaks centered at the binding energy of 531.9 and 533.3 eV, which were assigned to S=O (or C=O) and C—O bond signals, respectively [47,49]. The S=O bond came from the doped BPS molecular, while the C=O originated from the intermediate isocyanic acid. The emergence of C—O bond signal in BS—CN could be attributed to the partial condensation of O-bonding aromatic rings [42]. The S 2p XPS spectrum (Fig. 2d) further confirmed the oxidized sulfur moieties in the BS—CN with the obvious peak at 167.7 eV [50].

Raman spectrum of BS-CN (Fig. S4a) showed similar characteristic peaks of g-C_3N_4 nanosheets at 706, 765, 977, 1114, 1479, 1576, and 1614 cm^{-1}, indicating the g-C_3N_4 skeleton maintained after BPS doping. The relative intensity change can be ascribed to the incorporation of the benzene ring [48,51]. In addition, no D or G band was observed, indicating the benzene rings were homogenously doped into g-C_3N_4 nanosheets without the formation of the large region consisting of the consecutive carbon rings.

Based on the above results, it can be concluded that the benzene-ring had been successfully incorporated in the skeleton of g-C_3N_4 through thermal co-polymerization strategy. The benzene-ring dopants were uniformly doped in g-C_3N_4 nanosheets, while the high surface area and basal structure of g-C_3N_4 were preserved, which made the BS-CN a potential photocatalyst.

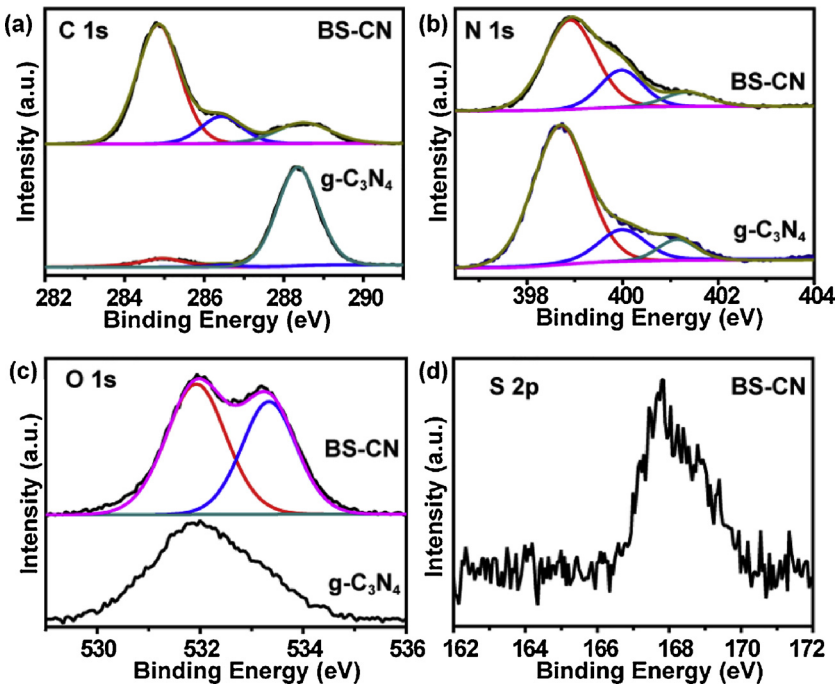

Fig. 2. (a) C 1s XPS spectra, (b) N 1s XPS spectra, and (c) O 1s XPS spectra of BS-CN and g-C_3N_4. (d) S 2p XPS spectra of BS-CN.

3.2. Optical and photocatalytic property of BS-CN

The optical properties of the catalysts were analyzed by UV–vis diffuse reflectance spectra. As shown in Fig. 3a, the adsorption edge of g-C_3N_4 nanosheets was around 440 nm. In comparison, the BS-CN remarkably extended the absorption up to near 800 nm with a darker yellow color in appearance (Fig. S5), which is benefit to improve the utilization of solar energy. The indirect band gap of BS-CN was estimated to be only 2.33 eV from the fitting Tauc plots. Notably, another liner regime (2.0–3.0 eV) in Tauc plots was observed for BS-CN, indicating the band gap of 1.12 eV (Fig. S6), which may be derived from the benzene ring [42]. The moderation of the band structure was also evidenced by the Mott-Schottky plots. The location of the conductive band minimum (CBM) of BS-CN deduced from flat band potential by Mott-Schottky plot was −0.89 V (vs Ag/AgCl; Fig. 4b), which was 0.33 V lower than that of pure g-C_3N_4 nanosheets (Fig. S7).

Photoluminescence (PL) spectra were also conducted (Fig. 3c). The broad and strong emission peak at 460 nm, corresponding to band gap of 2.70 eV, indicating the strong combination of the electrons at the CBM and holes at the VBM of g-C_3N_4 nanosheets. In contrast, BS-CN showed a much weaker PL emission peak and shifted to a longer wavelength (ca. 510 nm), indicating the effective separation of electrons and holes through incorporation of benzene-ring structure. The time-resolved fluorescence decay spectra (Fig. 3d) showed a distinctly slower decay for BS-CN, also demonstrating the improved charge separation. The calculated average lifetime for BS-CN was 18.51 ns, almost 40% longer than that of g-C_3N_4 (11.14 ns) (Table S2). The EIS tests (Fig. S8) was conducted to study the charge transfers resistance of BS-CN and g-C_3N_4 by the semicircle in the low-frequency zone. An obvious decrease Nyquist plots diameter for BS-CN was observed, indicating the improved electron transfer kinetics in the PHE process through benzene-ring doping. Photocurrent response measurement (Fig. 3e) also

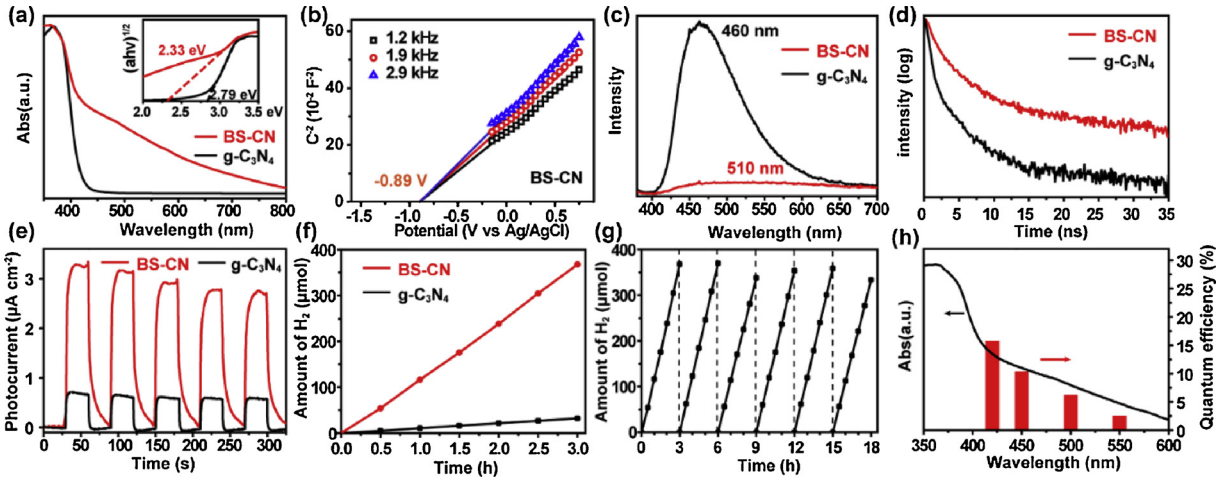

Fig. 3. (a) UV–vis absorption spectra of BS-CN and g-C_3N_4 nanosheets. (b) Mott–Schottky plots of BS-CN at the selected frequencies of 2.9, 1.9, and 1.2 kHz. (c) Static fluorescence emission spectra, (d) time-resolved fluorescence decay spectra, (e) photocurrent curves, and (f) the photocatalytic H_2 evolution activities of BS-CN and g-C_3N_4 nanosheets. The inset of (a) shows the band gap Tauc plots. (g) The reusability and (h) quantum efficiency vs. wavelength of. BS-CN (For interpretation of the references to colour in the text the reader is referred to the web version of this article).

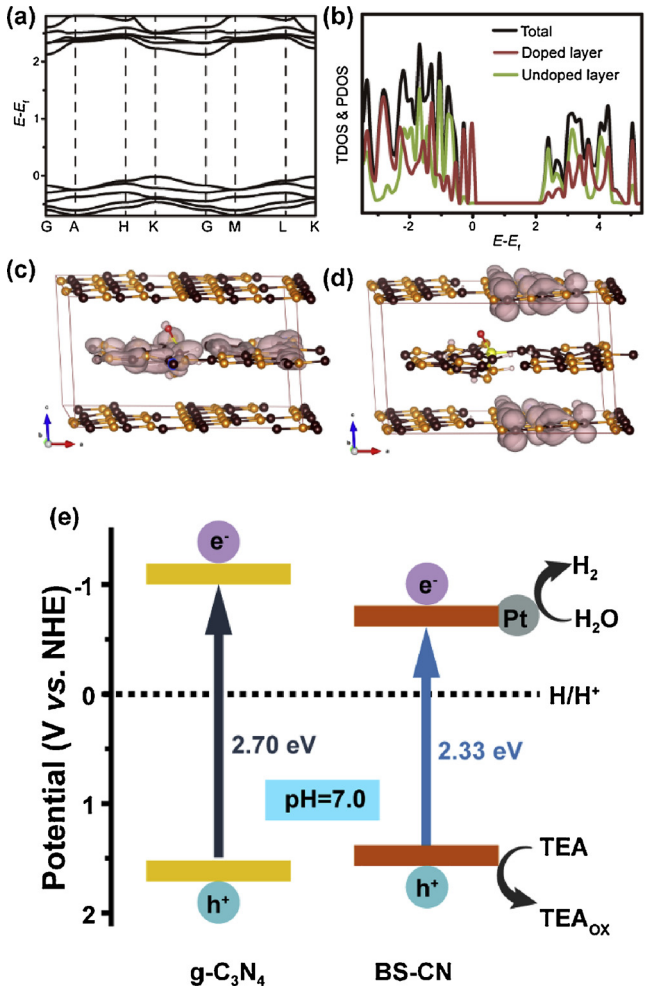

Fig. 4. (a) The calculated band dispersion and (b) TDOS and PDOS profiles of BS-CN. The band-decomposed charge-density distribution at (c) VBM and (d) CBM of BS-CN. (e)The diagrammatic comparison of band structures of g-C_3N_4 and. BS-CN.

confirmed the fast transfer of the carriers in BS-CN. The doped material BS-CN showed 5 times higher photocurrent than that of pure g-C_3N_4 nanosheets. Therefore, all the above results indicated that BS-CN exhibited extended photo absorption, effective charge separation, and fast charge transfer, which made it a promising material in the photocatalytic reactions.

To evaluate the photocatalytic activity, the visible-light-driven hydrogen evolution reactions were tested in the co-existence with Pt co-catalyst and triethanolamine sacrificial agent. As shown in Fig. 3f, only 32 μmol H_2 was detected after 3 h irradiation when pure g-C_3N_4 nanosheets were used as the photocatalyst. Strikingly, 370 μmol H_2 was generated with BS-CN as the photocatalyst under the same reaction conditions. The calculated hydrogen evolution rate was 12.33 mmol h^{-1} g^{-1} for BS-CN, which was almost 12 times higher than that of pure g-C_3N_4 nanosheets (1.07 mmol h^{-1} g^{-1}). Compared with the recent literatures (Table S3), BS-CN also showed excellent photocatalytic activity. Furthermore, the quantum efficiency (QE, 100 mg catalyst) was measured at 420 ± 15, 450 ± 15, 500 ± 15, and 550 ± 15 nm. The results matched well with the absorption value in the whole wavelength region (Fig. 3h). It was worth noting that the highest QE of 17.7% was obtained at 420 nm, which was among the excellent results in the literatures (Table S3). Besides the high activity and QE, the obtained BS-CN also showed satisfied stability even after six cycles in 18 h (Fig. 3g). After photocatalytic test, TEM, SEM, FT-IR, XRD, and NMR measurements of the catalyst were performed and the results were showed in Fig. S9. There was no obvious difference between the fresh and used BS-CN in the above tests, indicating the good stability of the benzene-ring doped catalysts.

It should be mentioned that the doping mount of BPS, pyrolysis temperature and time had some effects on the catalytic performance of the obtained BS-CN. The results were shown in Figs. S10–S12. It can be seen that the BS-CN obtained under the condition (25 mg of BPS, 500 °C for 2 h) was optimized, which can maximize the enhancement effect of the BPS doping. Over doping may destroy the basal structure of g-C_3N_4. Higher etching temperature or longer etching time may also cause destruction of the material, resulting in the lower catalytic performance.

3.3. DFT calculations

To reveal the relationship between the doping unit and the excellent photocatalytic ability in depth, the theoretical calculations of energy and electronic structure were carried out with Vienna ab-initio simulation package (VASP) [43,44]. As shown in Fig. 4a, the BS-CN showed the property of an indirect gap semiconductor with the Eg of 2.20 eV, about 0.4 eV smaller than g-C_3N_4 nanosheets (2.58 eV, Fig. S14a). The calculated Eg of the two samples was quite accordant to the results from experimental Tauc plots derivation (Fig. 3a). The partial density of state (PDOS) profiles (Fig. 4b) revealed that the frontier of valence band (VB) of BS-CN was preponderantly dominated by the orbitals from the doped layer, while the frontier of conductive band (CB) was mainly constituted by the electronic states originated from the undoped layer. This characteristic was agreed with the analysis of band-decomposed charge-density distributions (BDCD). The BDCD of BS-CN at the valence band maximum (VBM, Fig. 4c) was mostly confined in the benzene ring-containing and the sulfur-bonding tri-s-triazene units, while the BDCD at conduction-band minimum (CBM, Fig. 4d) was located at the undoped layer. It was well known that the BDCD at CBM and VBM of g-C_3N_4 nanosheets (Figs. S14c–d) were localized at the adjacent atoms in the same unit [42,52], resulting in a high recombination tendency of photo-induced carriers. In contrast, the photoinduced holes and electrons in BS-CN would be located at separate regions, mitigating the recombination of the charge carriers, which was verified by the remarkable enhancement in photocurrent and distinct decline in PL emission.

According to the above results, the diagrammatic comparison of band structure of BS-CN was drawn in Fig. 4e. With a narrower band gap, BS-CN can harvest more visible-light photons than g-C_3N_4 nanosheets. The separated CBM and VBM regions facilitate the transfer and separation of the photo-induced holes and electrons. The electrons reduce H^+ to hydrogen while the holes are consumed by TEA. Hence, the BPS doped g-C_3N_4 nanosheets showed much better hydrogen evolution performance than pure g-C_3N_4 nanosheets.

4. Conclusions

In summary, we designed a facile strategy to prepare benzene-ring doped g-C_3N_4 nanosheets for photocatalytic hydrogen evolution. Based on the experimental and theoretical results, the doped g-C_3N_4 nanosheet catalyst exhibited extended light adsorption and enhanced separation/transfer of photoinduced holes and electrons, which promoted it an excellent visible-light-driven PHE catalyst by 12-fold improvement. This work broadens new opportunities to design and fabricate highly active PHE catalyst.

Acknowledgements

We thank the financial supports from the National Natural Science Foundation of China (NSFC 21333009, 21573244, 21503013), Chinese Academy of Sciences-Peking University Pioneer Cooperation Team and the Youth Innovation Pro-motion Association of CAS (2017049).

Appendix A. Supplementary data

Supplementary material related to this article can be found, in the online version, at doi:https://doi.org/10.1016/j.apcatb.2018.11.070.

References

[1] A. Fujishima, K. Honda, Nature 238 (1972) 37–38.
[2] M.G. Walter, E.L. Warren, J.R. McKone, S.W. Boettcher, Q. Mi, E.A. Santori, N.S. Lewis, Chem. Rev. 110 (2010) 6446–6473.
[3] J. Zhang, J. Yu, M. Jaroniec, J.R. Gong, Nano Lett. 12 (2012) 4584–4589.
[4] L. Ye, J. Liu, C. Gong, L. Tian, T. Peng, L. Zan, ACS Catal. 2 (2012) 1677–1683.
[5] Q. Xiang, J. Yu, M. Jaroniec, J. Am. Chem. Soc. 134 (2012) 6575–6578.
[6] T.-D. Nguyen-Phan, S. Luo, D. Vovchok, J. Llorca, J. Graciani, J.F. Sanz, S. Sallis, W. Xu, J. Bai, L.F.J. Piper, D.E. Polyansky, E. Fujita, S.D. Senanayake, D.J. Stacchiola, J.A. Rodriguez, ACS Catal. 6 (2015) 407–417.
[7] F.E. Osterloh, Chem. Soc. Rev. 42 (2013) 2294–2320.
[8] X. Jiang, P. Wang, J. Zhao, J. Mater. Chem. A 3 (2015) 7750–7758.
[9] Z. Sun, H. Zheng, J. Li, P. Du, Energy Environ. Sci. 8 (2015) 2668–2676.
[10] H. Li, Y. Sun, Z.Y. Yuan, Y.P. Zhu, T.Y. Ma, Angew. Chem. Int. Ed. 57 (2018) 3222–3227.
[11] X. Wang, K. Maeda, A. Thomas, K. Takanabe, G. Xin, J.M. Carlsson, K. Domen, M. Antonietti, Nat. Mater. 8 (2009) 76–80.
[12] S. Cao, J. Yu, J. Phys. Chem. Lett. 5 (2014) 2101–2107.
[13] Q. Han, B. Wang, J. Gao, Z. Cheng, Y. Zhao, Z. Zhang, L. Qu, ACS Nano 10 (2016) 2745–2751.
[14] S. Yang, Y. Gong, J. Zhang, L. Zhan, L. Ma, Z. Fang, R. Vajtai, X. Wang, P.M. Ajayan, Adv. Mater. 25 (2013) 2452–2456.
[15] P. Niu, L. Zhang, G. Liu, H.-M. Cheng, Adv. Funct. Mater. 22 (2012) 4763–4770.
[16] N. Meng, J. Ren, Y. Liu, Y. Huang, T. Petit, B. Zhang, Energy Environ. Sci. 11 (2018) 566–571.
[17] H. Ou, P. Yang, L. Lin, M. Anpo, X. Wang, Angew. Chem. Int. Ed. 56 (2017) 10905–10910.
[18] Q. Han, B. Wang, Y. Zhao, C. Hu, L. Qu, Angew. Chem. Int. Ed. 54 (2015) 11433–11437.
[19] Q. Han, Z. Cheng, J. Gao, Y. Zhao, Z. Zhang, L. Dai, L. Qu, Adv. Funct. Mater. 27 (2017) 1606352.
[20] S. Guo, Z. Deng, M. Li, B. Jiang, C. Tian, Q. Pan, H. Fu, Angew. Chem. Int. Ed. 55 (2016) 1830–1834.
[21] Z.-F. Huang, J. Song, X. Wang, L. Pan, K. Li, X. Zhang, L. Wang, J.-J. Zou, Nano Energy 40 (2017) 308–316 7.
[22] J. Li, B. Shen, Z. Hong, B. Lin, B. Gao, Y. Chen, Chem. Commun. 48 (2012) 12017–12019.
[23] J. Hong, X. Xia, Y. Wang, R. Xu, J. Mater. Chem. 22 (2012) 15006–15012.
[24] G. Liu, P. Niu, C. Sun, S.C. Smith, Z. Chen, G.Q. Lu, H.-M. Cheng, J. Am. Chem. Soc. 132 (2010) 11642–11648.
[25] T.Y. Ma, J. Ran, S. Dai, M. Jaroniec, S.Z. Qiao, Angew. Chem. Int. Ed. 54 (2015) 4646–4650.
[26] J. Ran, T.Y. Ma, G. Gao, X.-W. Du, S.Z. Qiao, Energy Environ. Sci. 8 (2015) 3708–3717.
[27] J.-W. Zhang, S. Gong, N. Mahmood, L. Pan, X. Zhang, J.-J. Zou, Appl. Catal. B Environ. 221 (2018) 9–16.
[28] M. Zhu, S. Kim, L. Mao, M. Fujitsuka, J. Zhang, X. Wang, T. Majima, J. Am. Chem. Soc. 139 (2017) 13234–13242.
[29] J. Liu, Y. Liu, N. Liu, Y. Han, X. Zhang, H. Huang, Y. Lifshitz, S.T. Lee, J. Zhong, Z. Kang, Science 347 (2015) 970–974.
[30] S.-W. Cao, Y.-P. Yuan, J. Fang, M.M. Shahjamali, F.Y.C. Boey, J. Barber, S.C. Joachim Loo, C. Xue, Int. J. Hydrogen Energy 38 (2013) 1258–1266.
[31] L. Ge, C.C. Han, Appl. Catal. B Environ. 117 (2012) 268–274.
[32] S.J.A. Moniz, S.A. Shevlin, D.J. Martin, Z.-X. Guo, J. Tang, Energy Environ. Sci. 8 (2015) 731–759.
[33] Y. Wang, W. Yang, X. Chen, J. Wang, Y. Zhu, Appl. Catal. B Environ. 220 (2018) 337–347.
[34] Y. Wang, W. Jiang, W. Luo, X. Chen, Y. Zhu, Appl. Catal. B Environ. 237 (2018) 633–640.
[35] H. Tian, M. Liu, W. Zheng, Appl. Catal. B Environ. 225 (2018) 468–476.
[36] X. Fan, L. Zhang, R. Cheng, M. Wang, M. Li, Y. Zhou, J. Shi, ACS Catal. 5 (2015) 5008–5015.
[37] M.K. Bhunia, K. Yamauchi, K. Takanabe, Angew. Chem. Int. Ed. 53 (2014) 11001–11005.
[38] Y. Yu, W. Yan, X. Wang, P. Li, W. Gao, H. Zou, S. Wu, K. Ding, Adv. Mater. 30 (2018) 1705060.
[39] W. Che, W. Cheng, T. Yao, F. Tang, W. Liu, H. Su, Y. Huang, Q. Liu, J. Liu, F. Hu, Z. Pan, Z. Sun, S. Wei, J. Am. Chem. Soc. 139 (2017) 3021–3026.
[40] W.H. Niu, K. Marcus, L. Zhou, Z. Li, L. Shi, K. Liang, Y. Yang, ACS Catal. 8 (2018) 1926–1931.
[41] M. Zhang, X. Wang, Energy Environ. Sci. 7 (2014) 1902–1906.
[42] Y. Yu, W. Yan, W. Gao, P. Li, X. Wang, S. Wu, W. Song, K. Ding, J. Mater. Chem. A 5 (2017) 17199–17203.
[43] G. Kresse, J. Furthmüller, Phys. Rev. B 54 (1996) 11169–11186.
[44] J. Heyd, G.E. Scuseria, M. Ernzerhof, J. Chem. Phys. 118 (2003) 8207–8215.
[45] F. Fina, S.K. Callear, G.M. Carins, J.T.S. Irvine, Chem. Mater. 27 (2015) 2612–2618.
[46] J. Zhang, G. Zhang, X. Chen, S. Lin, L. Mohlmann, G. Dolega, G. Lipner, M. Antonietti, S. Blechert, X. Wang, Angew. Chem. Int. Ed. 51 (2012) 3183–3187.
[47] J. Liu, T. Zhang, Z. Wang, G. Dawson, W. Chen, J. Mater. Chem. 21 (2011) 14398–14401.
[48] Q. Xiang, J. Yu, M. Jaroniec, J. Phys. Chem. C 115 (2011) 7355–7363.
[49] Y.-N. Zhu, C.-Y. Cao, W.-J. Jiang, S.-L. Yang, J.-S. Hu, W.-G. Song, L.-J. Wan, J. Mater. Chem. A 4 (2016) 18470–18477.
[50] L.Y. Li, W. Fang, P. Zhang, J.H. Bi, Y.H. He, J.Y. Wang, W.Y. Su, J. Mater. Chem. A 4 (2016) 12402–12406.
[51] J. Jiang, L. Ou-yang, L. Zhu, A. Zheng, J. Zou, X. Yi, H. Tang, Carbon 80 (2014) 213–221.
[52] W. Yan, Y. Yu, H. Zou, X. Wang, P. Li, W. Gao, J. Wang, S. Wu, K. Ding, Solar RRL, (2018), p. 1800058, https://doi.org/10.1002/solr.201800058.